THE ASTROPHYSICAL JOURNAL, 473:L115–L118, 1996 December 20

A SEARCH FOR THE OPTICAL COUNTERPART OF THE TRIPLE PULSAR SYSTEM PSR B1620−26 IN M4[1]

A. SHEARER, R. BUTLER, AND R. M. REDFERN
Department of Experimental Physics, University College Galway, Galway, Ireland
M. CULLUM
European Southern Observatory, Karl-Schwarzchild-Strasse 2, D-85748 Garching bei München, Germany
AND
A. C. DANKS
Hughes STX/NASA Goddard Space Flight Center, Code 683.0, Greenbelt, MD 20771
Received 1996 June 18; accepted 1996 October 7

ABSTRACT

We have performed photometry in B and V of the field of the triple system PSR B1620−26 in the globular cluster M4. Our images were taken with two two-dimensional imaging photon-counting detectors, which permitted deep exposures to be made without saturation. Photometry of the proposed optical counterpart of the second companion of PSR B1620−26 was obtained, yielding a magnitude $V = 21.30 \pm 0.08$ and a color $B - V = 1.32 \pm 0.20$. The color index has not been successfully determined previously. These values locate the counterpart on the main sequence of the cluster color-magnitude diagram and lead to a mass determination that is consistent with a 0.48 $M_\odot$ cluster main-sequence star.

Subject headings: binaries: close — globular clusters: individual (M4) — pulsars: individual (PSR B1620−26) — techniques: photometric

1. INTRODUCTION

The existence of binary systems in globular clusters (GCs) has theoretically been predicted to halt core collapse and, possibly, to provide sufficient kinetic energy to thermally reexpand the core. Only a few binary systems have been observed in GC cores, and only one triple system, that associated with the 11 ms pulsar B1620−26. This pulsar is in a nearly circular orbit ($e = 0.0253$) with a companion of mass $\approx 0.3\ M_\odot$. As well as this comparatively large value for the orbital eccentricity, the pulsar period has a high second derivative, $\sim 10^7$ times larger than the expected value and of the wrong sign if purely due to the expected spin-down of the pulsar. This additional source of acceleration could be due to a third component of either stellar or planetary mass (Backer, Foster, & Sallmen 1993; Thorsett, Arzoumanian, & Taylor 1993). Conventional models for the creation of a millisecond pulsar involve the spin-up by mass transfer onto a slower neutron star from a low-mass companion. This process would lead to the formation of a low-mass white dwarf companion. At the distance of M4 such a star would not be visible. For example, the companion to PSR J0437−4715, a nearby neutron star/low-mass white dwarf binary system (Bailyn 1995), would have a visual magnitude of ∼27 in M4.

Bailyn et al. (1994, hereafter B94) obtained a total of 114 CCD frames of M4, 39 of which were in B and 75 in V. The seeing in their averaged images was $\approx 1\farcs5$ FWHM. Their reductions revealed a $V = 20.04$ mag stellar image of asymmetric shape within $0\farcs3$ of the nominal pulsar position. There was also an error of $0\farcs25$ between the radio and optical coordinate systems. The B magnitude was too uncertain to calculate a reliable $B - V$ index for their suggested optical counterpart, but assuming it to be a cluster main-sequence star yielded a mass of $\approx 0.45\ M_\odot$. Clearly there was a need for both higher resolution images of this field and for more precise photometry, to resolve more precisely the counterpart, to determine its color, and to search for other possible counterparts.

2. THE MINI-TRIFFID CAMERA AND OBSERVATIONS

Observations of M4 were made in 1995 February using the Mini-TRIFFID camera mounted upon the Nasmyth focus of the 3.5 m New Technology Telescope in La Silla, Chile. The camera, a simplified version of the TRIFFID camera (Redfern 1991), consists of a multianode microchannel array (MAMA) two-dimensional photon-counting detector and a fast recording system. In TRIFFID, the position and time of arrival of each photon are recorded and analyzed off-line to create images that do not suffer from saturation, blooming, and other limitations inherent in using a CCD to observe the core of a GC. The camera system was originally designed to be used to perform postexposure image sharpening, where the telescope pupil would be reduced to a diameter matched to the available seeing. However, for these observations, the depth of the images was a more important consideration than attaining the highest possible resolution, as the stellar crowding is relatively low in the core of M4. Therefore the telescope was operated at full aperture, which precluded any significant postexposure image sharpening.

Observations were made with two MAMA detectors, the ESO-MAMA (Cullum & Wampler 1990; Timothy & Bybee 1985) and the GSFC-MAMA (Danks et al. 1996), on two separate nights. The ESO-MAMA detector has a 1024×256 pixel format with a bi-alkali photocathode. The GSFC-MAMA is a ground-based observing MAMA, a small-format (960×224 pixels) version of the Space Telescope Imaging Spectrograph (STIS) detectors but equipped with an S20 photocathode for ground use. The system was built to test STIS proposed capabilities such as time-tag operation. The STIS detectors from which this tube is modeled are described by Danks et al. (1992, 1996). A mask, which reduced the field of view, was used to reduce the overall count rate from the more sensitive GSFC-MAMA. The pixel scale was $0\farcs13$ pixel^{-1}. Conditions were photometric for all the observations.

[1] Based upon observations collected at the European Southern Observatory, La Silla, Chile.

TABLE 1

OBSERVATION LOG

Date	Exposure (s)	Detector	Filter	Seeing (arcsec)
1995 Feb 26	3003	GSFC	*B*	0.81
1995 Feb 27	1849	ESO	*B*	0.91
1995 Feb 27	2618	ESO	*V*	0.57

Table 1 shows a log of the observations. They were specifically designed to be efficient in locating the PSR 1620−26 candidate and its neighbors on the cluster color-magnitude diagram (CMD). The two deep exposures in *B* were necessary to show the cluster main sequence clearly down to 20th magnitude and, by extrapolation, to fainter magnitudes.

3. DATA REDUCTION

3.1. *Initial Reduction*

The photon data in each exposure were shift-and-add sharpened and flat-fielded to produce integrated CCD-like images, using software developed in Galway (Obyrne et al. 1991; Morris 1995). Because the telescope was operated at full aperture, a significant degree of resolution improvement over the prevailing long-exposure seeing would not be expected; but the removal of telescope wobble typically yielded a 20% resolution improvement, with subsequent benefits to star detection and photometry. The final resolution of the three images is also indicated in Table 1. A shifted and scaled dark frame was then subtracted from the GSFC-MAMA *B* image; the ESO-MAMA has essentially zero dark counts within the exposure times utilized, and thus no correction was required for the other two images. The upper three panels of Figure 1 (Plate L17) show the three final images, with the position of PSR 1620−26 circled on each.

3.2. *Photometric Reduction*

Using the implementation of DAOPHOT2 (Stetson 1994) in the external IRAF package DAOPHOTX, standard photometric reductions were first performed on the images, each with its own self-determined star list, until an accurate point-spread function (PSF) was computed for each. The PSFs were spatially invariant, consisting of an analytic Moffat function plus one lookup table of residuals. Each image and its PSF were then fed into an STSDAS MEM maximum entropy restoration (Wu 1994); a small number of MEM iterations was chosen to avoid overfitting and background noise amplification. The bottom panel of Figure 1 shows the MEM-restored *V* image. Although not photometrically reliable, two crucial benefits accrued from the enhanced resolution of the MEM-restored images. First, the restored *V* image, with its better initial seeing and greater depth down the main sequence, was used to determine the most complete star list possible. Second, it was now possible to employ the routines in the external IRAF package IMMATCH to accurately coordinate-transform this master star list to the *B* images, by using 70–150 common stars on the MEM-restored images to map full third-order geometric transformations. The rms transformation residuals for these stars were of order 0.″02.

After these steps, IRAF DAOPHOTX was used again to recompute PSFs for each image and to fit and subtract all the stars in the master star list. Because of the variable reddening toward M4 (Dixon & Longmore 1993), standardizing of the instrumental magnitudes was accomplished by adopting the parameters of Kanatas et al. (1995); errors in the zero points of ∼0.1 mag are possible but do not impact on our discussion below.

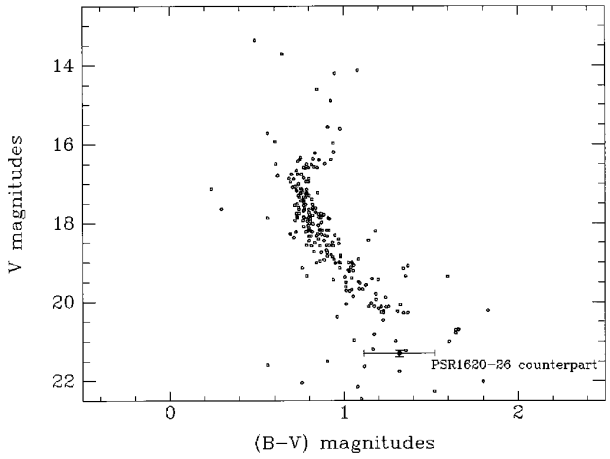

FIG. 2.—Color-magnitude diagram of M4 field

4. DISCUSSION

Figure 2 shows the (nondereddened) CMD of the field around PSR 1620−26. This only shows those stars that were well measured on all three images. We shall now explain what constitutes a "well-measured" star. First, any star that was common to all three images but lying near the edge of any one has not been included, as its measurement is likely skewed by unsubtracted stars whose centers lie just off the edge of that image. Inspection of the DAOPHOTX CHI and SHARP statistics supports this approach. Second, an acknowledged problem with ALLSTAR in DAOPHOTX is that, while allowing the stars to be recentered during the profile fitting, the positions of some of the faintest stars may be greatly shifted to peaks in the subtraction noise of nearby very bright stars, thereby increasing the scatter in the CMD. On the other hand, switching off recentering does not yield an optimal fit to many of the stars, because of small residual errors in the coordinate transformation (due to image-plane distortions and localized seeing variations after image sharpening). We therefore performed photometry on the *B* images both with and without recentering and took the recentered measurements as the final values for each star unless its position had been shifted by more than 0.5 pixel (well outside the possible error in the coordinate transformations), in which case we used the nonrecentered measurements.

The *B* measurements were then averaged before calculating the $B - V$ index. The averaging was weighted by the relative depth of the two exposures in *B*, as the longer exposure with the more sensitive GSFC-MAMA had detected 3.7 times the amount of flux per star compared with the ESO-MAMA exposure. Together with the slightly better seeing on the GSFC-MAMA image, this greater depth led to superior photometry of the fainter stars in the field, an advantage that was preserved by the weighted averaging. However, this approach yields no such advantage for the photometry of stars in the upper portion of the CMD, where the Poissonian errors are very low; in fact, the deeper flat fields we had recorded for the ESO-MAMA permitted slightly better photometry in this regime, with the result that weighting the averages toward the GSFC-MAMA photometry actually broadens somewhat the color spread in the upper portion of the CMD. This is an acceptable drawback because we are primarily interested in optimal photometry of the fainter regime.

We noted that the brightest few stars in the full field, at the

TABLE 2

STARS WITHIN 6″ OF THE NOMINAL PULSAR POSITION MEASURED ON ALL THREE IMAGES

ID	Position		Magnitude on Each Image				
	East (arcsec)	North (arcsec)	V (mag)	B_{ESO} (mag)	B_{GSFC} (mag)	B_{av} (mag)	$B - V$ (mag)
147	4.54	−0.69	18.23 ± 0.01	18.99	18.93	18.95	0.72 ± 0.01
171	3.42	−4.72	17.07 ± 0.00	17.80	17.78	17.79	0.72 ± 0.01
172	3.76	−1.08	18.73 ± 0.01	19.59	19.54	19.56	0.83 ± 0.02
195	3.23	−0.17	19.86 ± 0.03	20.85	20.94	20.91	1.05 ± 0.04
219	2.68	−0.73	18.84 ± 0.01	19.77	19.73	19.75	0.91 ± 0.02
230	2.77	1.75	17.55 ± 0.00	18.29	18.25	18.26	0.72 ± 0.01
238	2.95	5.14	18.85 ± 0.02	19.83	19.84	19.84	0.98 ± 0.03
273	0.88	−5.46	17.51 ± 0.00	18.24	18.25	18.25	0.73 ± 0.01
280	1.86	5.13	19.69 ± 0.05	20.71	20.83	20.79	1.11 ± 0.08
317	0.58	1.41	20.22 ± 0.05	21.64	22.26	22.05	1.83 ± 0.16
341	−0.55	−2.81	20.99 ± 0.06	21.85	22.51	22.29	1.30 ± 0.11
342	0.19	5.02	14.20 ± 0.00	15.22	15.11	15.15	0.95 ± 0.00
349	−0.91	−4.64	17.09 ± 0.00	17.79	17.80	17.80	0.71 ± 0.01
350	**−0.33**	**0.32**	**21.30 ± 0.08**	**21.82**	**23.04**	**22.62**	**1.32 ± 0.20**
359	−0.70	1.69	16.40 ± 0.00	17.24	17.26	17.25	0.86 ± 0.00
415	−2.84	−5.27	16.67 ± 0.00	17.40	17.40	17.40	0.73 ± 0.01
442	−2.99	−0.11	18.17 ± 0.01	19.06	19.02	19.03	0.86 ± 0.01
443	−2.76	1.73	22.04 ± 0.16	23.51	22.43	22.80	0.76 ± 0.30
444	−2.26	3.97	16.43 ± 0.00	17.26	17.12	17.17	0.74 ± 0.01
1666	−2.48	3.49	18.41 ± 0.04	19.62	19.26	19.38	0.97 ± 0.06
1696	−0.11	1.62	19.16 ± 0.05	21.58	19.94	20.50	1.34 ± 0.12

level of the horizontal branch, appear to be 0.1–0.2 mag too faint in V and too blue in $B - V$ by the same amount. This resulted from slight localized nonlinearities in the detector behavior, arising under the high local photon-event rates sustained when operating in excellent seeing with the broad-band V filter and the full 3.5 m aperture of the telescope. Inspection of the DAOPHOTX CHI and SHARP statistics confirmed that a nonlinear response altered the core profiles of these few particular stars. This is further evidenced in Figure 3 by the residuals left after subtraction of the three brightest stars on this section of the V image. However, we stress that this has no bearing on the photometry of stars fainter than $V \approx 14$.

We measured 21 stars, on all three images, that lie within 6″ of the pulsar position. The positions, individual magnitude determinations, and colors of these 21 stars are listed in Table 2. Star 350 corresponds to the B94 optical counterpart of PSR 1620−26.

From Table 2 and the CMD, it is clear that the B94 optical counterpart of PSR 1620−26 is located on or near the cluster main sequence. This is the first time that its color ($B - V = 1.32 \pm 0.20$) has been determined. At $V = 21.30 \pm 0.08$, it is 1.26 mag fainter than the determination of B94, who also used DAOPHOT2 to perform the photometry on their low-resolution CCD images. There are no relative zero-point errors, between the sources used to calibrate the two sets of photometric results, that can explain such a large discrepancy—Kanatas et al. (1995) give V(HB) = 13.50, for example, in close agreement with the V(HB) = 13.45 given by Cudworth & Rees (1990). However, the discrepancy is understandable in light of the known tendency of both DAOPHOT and DAOPHOT2 to overestimate the magnitudes of stars near the signal-to-noise limit (Debray et al. 1994), a limit that was set by the poor, uncorrected seeing in the case of B94. This tendency is also illustrated in Table 2 by the fact that the magnitude of the counterpart determined from the ESO-MAMA B image is much brighter than that determined from the GSFC-MAMA B image, which was both deeper and sharper. Thus we found that the CMD with the lowest scatter for faint stars was that produced by the weighted-averaging approach described above, and it should be noted that the dominant source of error in the color of the counterpart is its low signal-to-noise ratio at $B \approx 22.5$, rather than the crowding with its bright neighbor (star 359). The error in V is also predominantly due to Poissonian signal-to-noise ratio, but at ±0.08 it is smaller than the estimated error in the zero-point calibration.

Figure 3 shows high-contrast gray-scale reproductions of identical sections of the original V image, the MEM-restored V image, and finally the original V image with all the stars subtracted except the optical counterpart. The circle marking the counterpart has the same size on the sky as that in Figure 1. Star 350 is 0.″4 from the nominal pulsar position, closer than any of the other detected stars. Table 2 gives astrometric information for these 21 stars within 6″ of the nominal pulsar position. Our astrometry was based upon the positions in B94, as our field of view was too restricted to include secondary astrometric standards. Thus the astrometric errors, with respect to the pulsar, for the stars in Table 2 are a function of three sources: the error estimated by B94 of 0.″25 between the radio and optical coordinate systems, the error in the transformation from the astrometry of B94 to our uncalibrated system, and the individual centroiding errors in our star positions. Even for faint stars, this third component is unlikely to be greater than 0.″02, because of the precautions taken with recentering when performing the photometry, as discussed above; we estimate the second component to be 0.″01 in right ascension and less than 0.″02 in declination, as these were the rms residuals of the transformation between our system and the eight stars whose astrometry is unaffected by blending in the B94 study. Summing these error components, we find that they may not entirely account for the 0.″4 difference between the nominal pulsar position and the position of star 350.

We adopt a distance modulus of 11.22, which, combined with an $E(B - V)$ of 0.37 (Dixon & Longmore 1993), yields a mass of $\approx 0.48\ M_{\odot}$ (Green, Demarque, & King 1987). We found that a value of [Fe/H] of −1.27 and an age of 17 Gyr yielded a best fit to our CMD. We also found that other isochrones (VandenBerg & Bell 1985; Bergbusch & VandenBerg 1992) do not change the mass determination significantly.

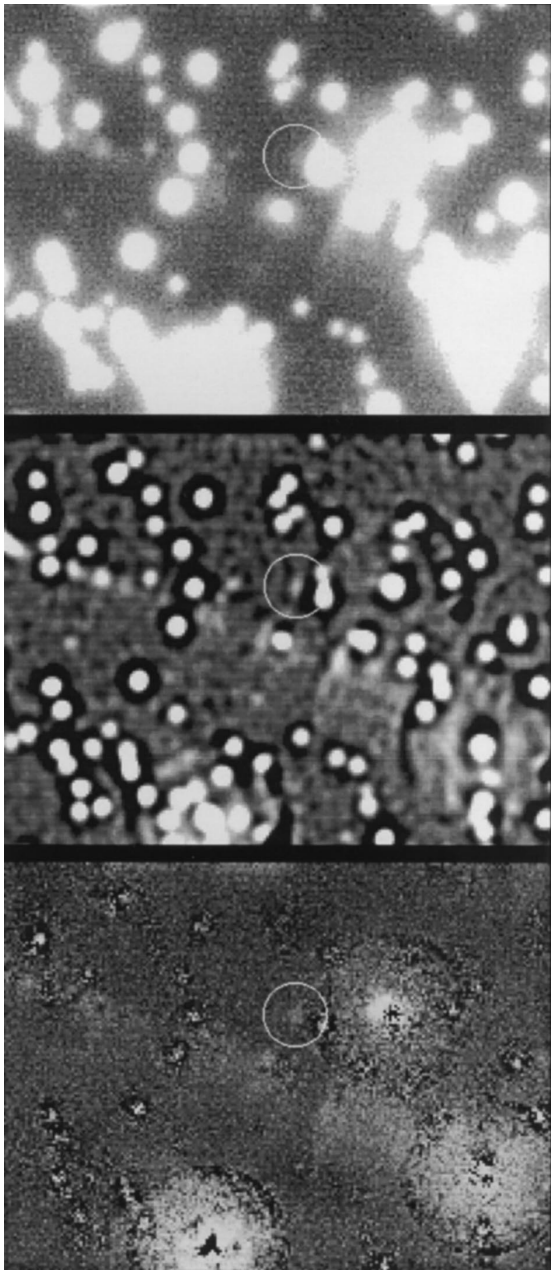

FIG. 3.—A 200 × 150 pixel (26″ × 19.″5) section of the ESO-MAMA *V* image. *Top to bottom*: High-contrast gray-scale reproductions of the original *V* image, the MEM-restored *V* image, and finally the original *V* image with all the stars subtracted except the optical counterpart. East is up, north is to the right. The circle marking the counterpart has the same size on the sky as that in Fig. 1. A faint strip of emission nebulosity appears to run diagonally across the image.

5. CONCLUSION

Our magnitude and color measurements of Bailyn et al.'s (1994) optical counterpart of PSR 1620−26 lead to a mass determination that is consistent with a 0.48 $M_\odot$ cluster main-sequence star. This is in contrast with the similar mass calculated by B94, using the same isochrones, for their star, which was 1.3 mag fainter. Their reduced magnitude can be understood in terms of the effects of blending in the earlier study. Our mass determination does not constrain the eccentricity of the orbit (Michel 1994), but it can be consistent with a large eccentricity, predicted by most evolution scenarios involving binary-binary or binary–single-star interactions (see Rasio, McMillan, & Hut 1995; Hut et al. 1992).

We measured 21 stars in both *B* and *V* within 6″ of the pulsar's position, compared with 16 in *V* from B94. With more stars near the pulsar, the probability increases that the optical counterpart candidate nearest to the pulsar's position is just a positional coincidence of an unassociated cluster member. From Monte Carlo simulations, based on the measured stellar density, we found that there was a probability of 0.09 that a star would be located within 0.″4 of the nominal pulsar position. This probability increases to 0.17 when we include in our simulations an extra 19 stars within 6″ of the pulsar position, which had been measured either in *V* only or in *V* but only once in *B*.

We have also demonstrated that two-dimensional photon-counting detectors can take observations in the core of a globular cluster without the saturation problems that would limit the use of CCDs. This will be important in future ground-based surveys of variability in crowded field regions. In particular, it will now be possible to survey, over a prolonged period, the core regions of dense globular clusters in order to look for close binary systems, such as dwarf novae, in outburst. To date, such surveys have only been possible in the outer regions of a cluster, where the density of binaries is expected to be low (see, e.g., Shara, Bergeron, & Moffat 1994). Using detectors like the MAMA, such surveys, in which prolonged observation as well as high resolution is required, will be possible into the center of a globular cluster, where the density of binaries should be high, using ground-based telescopes.

We would like to thank the Irish Development Agency FORBAIRT for their support of this work under grant 930896. Paulo Garcia is thanked for his help during the taking of these observations. The European Southern Observatory and NASA Goddard Space Flight Center are thanked for the provision of their MAMA detectors. We are grateful to François Ochsenbein of CDS, Strasbourg, for specially making the Revised Yale Isochrone electronic data available to us.

REFERENCES

Backer, D. C., Foster, R. S., & Sallmen, S. 1993, Nature, 365, 817
Bailyn, C. D. 1995, ApJ, 411, L83
Bailyn, C. D., Rubinstein, E. P., Girard, T. M., Dinescu, D. I., Rasio, F. A., & Yanny, B. 1994, ApJ, 433, L89 (B94)
Bergbusch, P. B., & VandenBerg, D. A. 1992, ApJS, 81, 163
Cudworth, K. M., & Rees, R. 1990, AJ, 99, 1491
Cullum, M., & Wampler, E. J. 1990, Messenger, 61, 58
Danks, A. C., Joseph, C., Bybee, R., Argebright, V., Abraham, J., Kimble, R., & Woodgate, B. 1992, in Proc. ESA Symp. on Photon Detectors for Space Instrumentation, ed. T. D. Guyenne & J. J. Hunt (ESA SP-356) (Paris: ESA), 269
Danks, A. C., et al. 1996, in Science with the *Hubble Space Telescope* II, ed. P. Benvenuti, F. D. Macchetto, & E. J. Schreier (Baltimore: STScI), 579
Debray, B., Llebaria, A., Dubout-Crillon, R., & Petit, M. 1994, A&A, 281, 613
Dixon, R. I., & Longmore, A. J. 1993, MNRAS, 265, 395
Green, E. M., Demarque, P., & King, C. R. 1987, The Revised Yale Isochrones and Luminosity Functions (New Haven: Yale University Obs.)
Hut, P., et al. 1992, PASP, 104, 681
Kanatas, I. N., Griffiths, W. K., Dickens, R. J., & Penny, A. J. 1995, MNRAS, 272, 265
Michel, F. 1994, ApJ, 432, 239
Morris, P. W. 1995, Univ. Coll. Galway Internal Software Rep. 95S
Obyrne, C., Jordan, B., O'Kane, P., Redfern, R. M., Shearer, A., & Wouts, R. 1991, Irish Astron. J., 20, 282
Rasio, F. A., McMillan, S., & Hut, P. 1995, ApJ, 438, L33
Redfern, R. M. 1991, Vistas Astron., 34, 201
Shara, M. M., Bergeron, L. E., & Moffat, A. F. J. 1994, ApJ, 429, 767
Stetson, P. B. 1994, PASP, 106, 250
Thorsett, S. E., Arzoumanian, Z., & Taylor, J. H. 1993, ApJ, 412, L33
Timothy, J. G., & Bybee, R. L. 1985, Proc. SPIE, 687, 1090
VandenBerg, D. A., & Bell, R. A. 1985, ApJS, 58, 561
Wu, N. 1994, in The Restoration of *HST* Images and Spectra—II, ed. R. J. Hanisch & R. L. White (Baltimore: STScI), 58

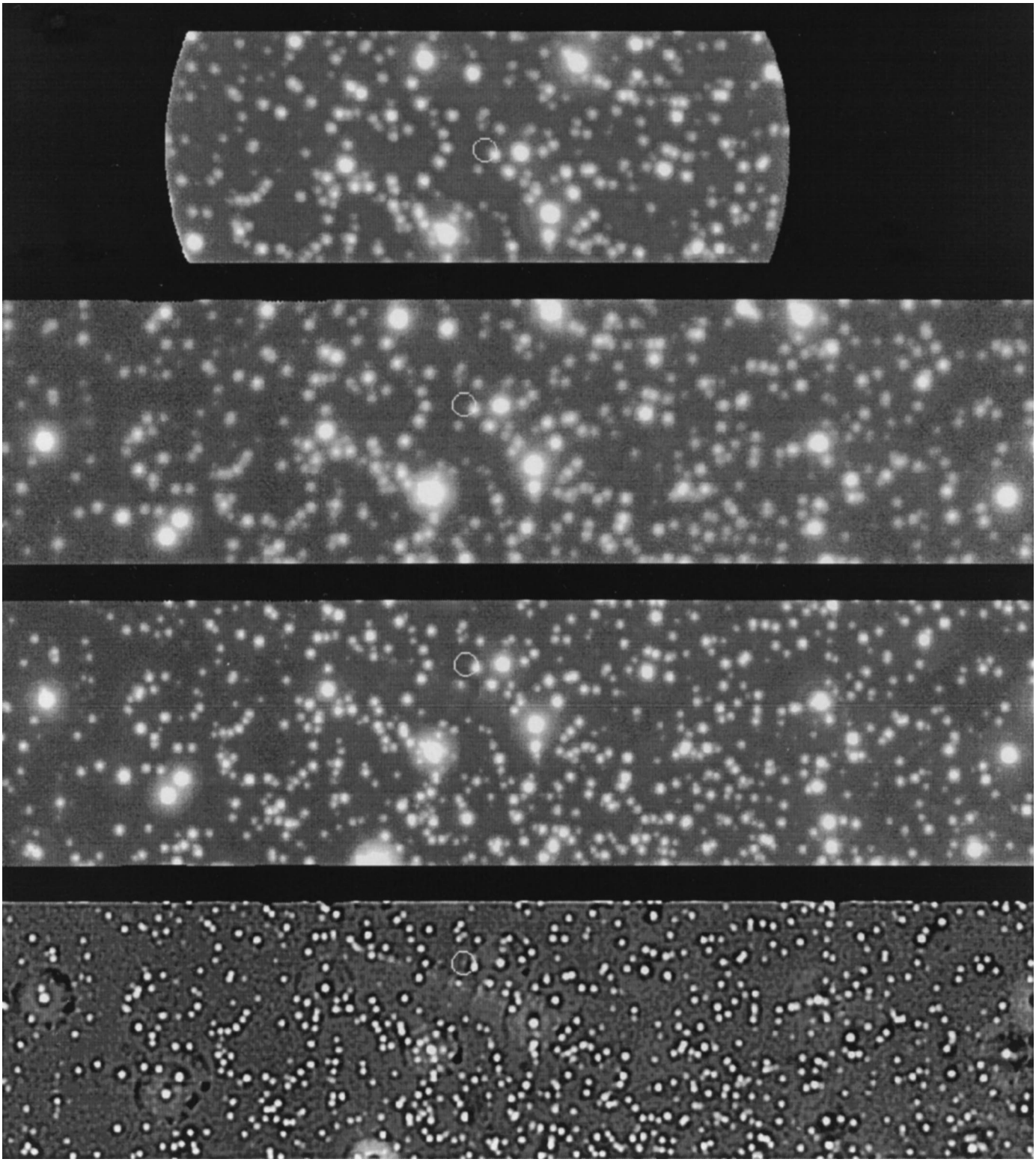

FIG. 1.—Full M4 field. *Top to bottom*: GSFC-MAMA in *B*, ESO-MAMA in *B*, ESO-MAMA in *V*, and MEM-restored image of the ESO-MAMA in *V*. The circle shows the position of PSR B1620−26.